Journal of Non-Newtonian Fluid Mechanics 169–170 (2012) 1–14

Contents lists available at SciVerse ScienceDirect

Journal of Non-Newtonian Fluid Mechanics

journal homepage: http://www.elsevier.com/locate/jnnfm

Laminar non-Newtonian impinging jet flow confined by sloping plane walls

A.S. Cavadas [a,*], F.T. Pinho [a], J.B.L.M. Campos [b]

[a] Centro de Estudos de Fenómenos de Transporte, DEMec, Faculdade de Engenharia da Universidade do Porto, Rua Dr. Roberto Frias s/n, 4200-465 Porto, Portugal
[b] Centro de Estudos de Fenómenos de Transporte, Departamento de Engenharia Química, Faculdade de Engenharia da Universidade do Porto, Rua Dr. Roberto Frias s/n, 4200-465 Porto, Portugal

ARTICLE INFO

Article history:
Received 6 October 2010
Received in revised form 9 September 2011
Accepted 18 October 2011
Available online 4 November 2011

Keywords:
Impinging jets
Non-Newtonian fluids
Separated flows
Laminar flow
Rectangular duct flow

ABSTRACT

An experimental investigation was carried out to characterize the flow field in a liquid impinging jet confined by inclined plane walls at an angle of 12° relative to the plate and emanating from a rectangular duct for two non-Newtonian fluids and a Newtonian reference fluid. The nozzle-to-plate distance (D) was kept constant at $D/H = 0.8$. The experiments were complemented by a numerical investigation for purely viscous generalized Newtonian fluids. Detailed measurements of mean flow fields were carried out by laser-Doppler anemometry at inlet duct Reynolds numbers of 200 pertaining to laminar flow regime and all flow fields were found to be symmetric relative to the x–y and x–z center planes. The two non-Newtonian fluids were aqueous solutions of xanthan gum (XG) and polyacrylamide (PAA) at weight concentrations of 0.2% and 0.125% respectively. A characteristic three-dimensional helical flow was seen to exist inside the recirculation, starting at the symmetry plane and spiraling to the flat side walls, which eliminated the separated flow region near these side walls, as previously found for Newtonian fluids [5]. Upon reaching the flat side wall region, the fluid in helical motion exits the recirculation and joins the main flow stream creating near-wall jets which were enhanced by the non-Newtonian fluid nature. The PAA solution, which was more elastic than the XG solution, was found to be subject to larger decelerations than the XG solution in the vicinity of the impinging plate. The numerical simulations investigated the roles of shear-thinning and inertia on the main flow characteristics for purely viscous fluids at Reynolds numbers between 10 and 800. The length of the recirculation (L_R) is constant in the central portion of the channel and decays to zero before reaching the flat side walls. At high Reynolds numbers a slight increase in L_R at the edge of the core of the flow is apparent. As expected, inertia increases the length of the recirculation as for Newtonian fluids, but somewhat surprisingly it also increases the three-dimensional nature of the flow by reducing the extent of the central core. Shear-thinning enhances the role of inertia especially at high Reynolds numbers, whereas at low Reynolds numbers the opposite behavior is observed.

1. Introduction

Confined impinging jets are frequently used to enhance heat and mass transfer since the high velocity fluid impinging the solid surface creates a very thin heat and/or mass boundary layer in addition to the beneficial effect of convective transport. Impinging jets are found in various industrial processes and systems such as in paper and textile drying, steel mills, tempering of glass, cooling of turbine blades and of electronic components. Hence, they have been the subject of many investigations to characterize the flow patterns, as well as the corresponding heat and mass transfer fluxes, and the relation between these fluxes and the geometric parameters and inlet flow conditions. Some early experimental contributions were those of Gardon and Akfirat [11,12] and of Korger and Krizek [16], amongst others. With the advent of accurate optical diagnostics in fluid mechanics such techniques as laser-Doppler anemometry (LDA) and more recently particle image velocimetry (PIV) became easily available and detailed experimental programs have extensively documented some basic flows.

Liquid single-phase impinging jets are usually either submerged or free-surface jets. In submerged jets, the liquid issues into a region containing the same liquid at rest, whereas in free-surface jets, the liquid jet is surrounded by ambient air or gas. Submerged jets can be unconfined or confined by a surface; in the latter case, there is usually a plate attached to the nozzle and more often than not the nozzle is parallel to the impinging surface. Narayanan et al. [21] investigated the flow pattern and heat transfer of plane impinging turbulent jets addressing specifically the effect of

* Corresponding author.
E-mail addresses: adelioc@fe.up.pt (A.S. Cavadas), fpinho@fe.up.pt (F.T. Pinho), jmc@fe.up.pt (J.B.L.M. Campos).

0377-0257/$ - see front matter © 2011 Elsevier B.V. All rights reserved.
doi:10.1016/j.jnnfm.2011.10.005

ejector clearance, which was varied between 3.5 and 5 hydraulic diameters. Chen and Modi [6] investigated also rectangular turbulent impinging jets aimed at quantifying the mass transfer rate.

Garimella and Rice [13] investigated circular jets confined by a conical wall. They divided the impinging jet flow field into the free-jet region, the impingement region and the wall region. In the free-jet region the flow is axial and is unaffected by the presence of the impinging plate. The axial velocity starts to decay at the nozzle exit, provided the nozzle-to-plate distance is not too small, and the jet spreads to the surroundings before the impingement.

Miranda and Campos [19,20], performed various studies in an impinging jet confined by a conical wall. Miranda and Campos [19] showed that the flow field and the mass transport in the conical cell were similar to those in a cylindrical cell (parallel confinement) and that the flow and the mass transfer characteristics could be divided into impact and wall zones. They showed the existence of a recirculation zone attached to the slopped wall (principal recirculation) and a second small recirculation zone at the impinging plate affecting considerably the flow in the exit when the flow was laminar.

Miranda and Campos [20] showed also that the use of impinging jets confined by a conical wall reduces the concentration polarization phenomenon in a membrane separation process. Since the solute accumulation in the mass boundary layer is reduced by the impact of the jet (thin mass boundary layer) and, in addition, by the stronger convective transport there is a decrease in the osmotic pressure with a consequent increase of the total pressure driving force relative to the corresponding membrane without jet. However they concluded that the contact area for separation by permeation is small in the conical geometry and suggested an improvement would result from the use of a rectangular geometry with confinement by inclined plane walls. Furthermore, most of the solutions to be permeated are polymeric solutions exhibiting a non-Newtonian rheological behavior. This behavior and the previous suggestion are the motivations to the present investigation.

It is clear from a careful survey of the literature, that in spite of the large body of work on confined impinging jets, there is a lack of information regarding planar impinging jets confined by inclined walls for Newtonian fluids and even more so when fluids have a non-Newtonian rheological behavior, thus setting the stage for the present experimental and numerical investigation. Here, the clearance between the duct and the plate is very short, at 20% of the duct height, and consequently the presence of the plate is felt inside the duct, as will be shown later. At the impingement region, the fluid strongly decelerates and is forced to change its direction, flowing to the cell exit after passing through the wall region where a boundary layer develops.

The remainder of this paper is organized as follows: the next section describes the experimental setup and the instrumentation used. This is followed by the presentation and discussion of the experimental results inside the upstream rectangular duct and in the impinging flow cell. Afterwards, before presenting results of a parametric numerical investigation, the numerical procedure is succinctly presented and the results of some simulations are compared with experimental data for the Newtonian and one non-Newtonian fluid (xanthan gum solution). All numerical simulations are for the Generalized Newtonian fluid model, where the viscosity is represented by the Carreau model, when comparing with experimental data, and by the power law when performing the parametric investigation on the effect of geometry variations on the impinging flow cell characteristics. Given the viscoelastic nature of the non-Newtonian fluids, it is important to refer that, simulations with viscoelastic models were attempted, but these never converged in this 3D flow. The paper closes with a summary of the main conclusions and an outline of future work.

2. Experimental rig and instrumentation

2.1. Experimental set-up

The flow loop used in the present experiments is shown schematically in Fig. 1. In the following description we refer to numbers in parenthesis identifying rig components, as in the figure. Flow was provided by a progressive cavity pump (2) (mono pumps Dresser model CB081AC1A3/G) fed directly from a stainless steel tank of 175 l of capacity (1). One pulsation damper (3), located immediately downstream of the mono pump outlet, was used to smooth out the flow and remove any pulsations prior to the inlet of the entrance reservoir (5). At the top of this reservoir, an air chamber dampened any residual pulsations in order to ensure a steady flow at the rectangular duct inlet. The 2.6 m long rectangular duct (6) was made of four modules and had an internal cross section area of 0.0052 m^2 (height (H) × width ($2*W$) = 0.02 m × 0.26 m, corresponding to an aspect ratio (AR) of 13). Each module was constructed from stainless steel plates, machined and ground to size and then assembled with screws and a bonding agent. Visual inspection did not show any misalignment or a step that could perturb the flow.

The origin of the coordinate system is located right in the middle of the rectangular duct exit cross-section, with x denoting the streamwise coordinate in the duct, y the transverse coordinate and z the spanwise coordinate. This coordinate system is drawn in Fig. 2, where the cell test section (7) is schematically represented. The test section has two inclined plane walls, each one making an angle of 12° relative to the flat surface (impinging plate), in order to confine the jet flow inside the cell. The fluid exits the test section through two symmetric thin vertical channels, each 4 mm thick (h) and having the same width as the inlet rectangular duct, thus defining an aspect ratio of 65 for the identical outlet channels. The reservoirs (5) and the cell (7) were made of acrylic to allow velocity measurements using a laser Doppler anemometer (LDA). The Roman numbering in Fig. 2b concerns the blocks used to build the computational meshes, as discussed in Section 5.1.

Eleven pressure taps were drilled along the rectangular duct x–y center plane, with 200 mm spacing between consecutive taps. They were used to study the development of the flow along the duct and in addition their results did not show any signs of misalignment between the duct modules (manufactured to within machine tolerances of ±10 μm), i.e., visual inspection of the rectangular duct and analysis of the pressure drop variation and LDA velocity measurements did not show any perturbation to the flow.

Pressure differences were measured by a differential pressure transducer, model P305D-S20 from Valydine. The transducer calibration was carried out in a device made up of two independent water columns with the water level checked by two precision rules with accuracy better than ±0.1 mm. All the pressure taps were drilled carefully to avoid spurious edge effects. For the design of pressure taps, the recommendations of Shaw [27] and Franklin and Wallace [10] were followed. The pressure measurements were essentially used to help determine whether the flow was fully-developed in the inlet duct.

An electromagnetic flowmeter, type Mag Master (4) from ABB Taylor, measured the volumetric flow rates ($\dot{Q}_{in}$) in the range of 0–5 l/s with an accuracy of ±0.2% of full scale.

All the instruments were connected to a PC provided with a data acquisition board interfaced with an Advantech PCLD-8115 card.

2.2. Laser-Doppler system

A 1-D laser-Doppler anemometer (LDA) from Dantec was used to measure the mean velocity fields. The LDA was used in the

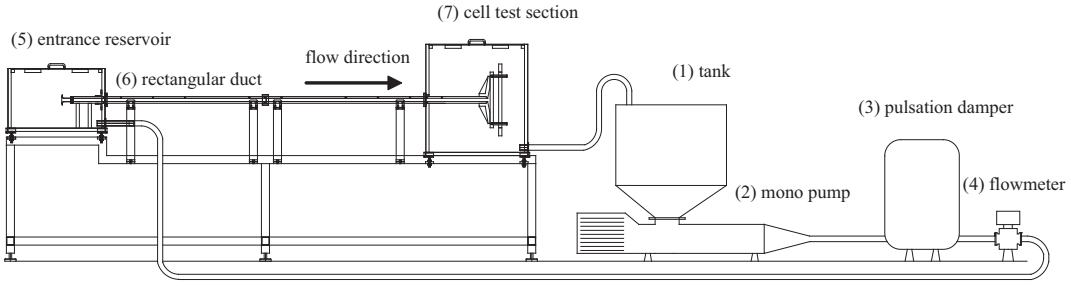

Fig. 1. Schematic representation of the flow loop.

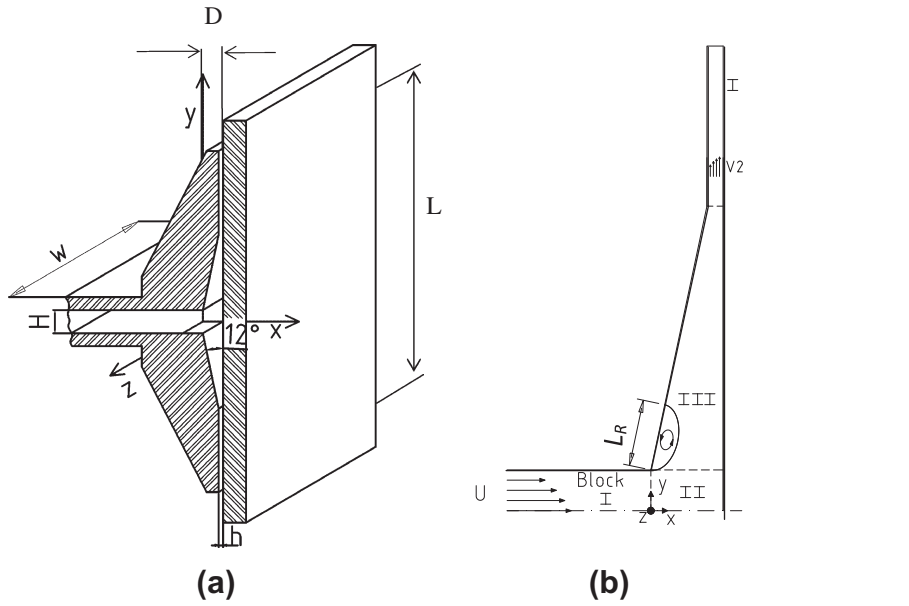

Fig. 2. Schematic representation of the cell test section and coordinate system centered in the *x*–*y* and *x*–*z* symmetry planes (a) only half the cell test section is shown; (b) a quarter of the cell test section is shown (the Roman numbers refer to the computational meshes).

forward scatter mode and the light source was an air-cooled, multimode 300 mW Ar-ion laser. The beam passed through a series of optical elements before the Bragg cell, where a frequency shift of 0.6 MHz was imposed. The front lens had a 300 mm focal length and the scattered light was collected by a photo-multiplier before which stood an interference filter of 514.5 nm. After being band-pass filtered, the signal from the photo-multiplier was processed by a TSI 1990C counter operating in the single measurement per burst mode with a frequency validation setting of 1% in the 10/16 cycle comparison. A 1400 Dostek card interfaced the counter with an 80486 based computer to provide all the statistical quantities via a purpose-built software. For each point measured, a sample size of 10,000 values was taken. The refraction of the laser beams at the plane walls of the duct and of the cell was taken into account to correct the position of the control volume. Table 1 provides the main characteristics of the LDA control volume.

The LDA probe was mounted on a milling table with movement in the three spatial coordinates. The system was used to measure the mean velocities in the horizontal (u) and vertical (v) directions along the duct and inside the cell. For the horizontal velocity component inside the rectangular duct the laser beams were set to cross each other in a horizontal plane. The milling table had a resolution of ±10 μm and the positioning of the LDA measuring volume in the channel is estimated to have a maximum total uncertainty of ±150 μm considering its various contributions and the control volume size in Table 1.

Table 1
Main characteristics of the LDA in air at e^{-2} intensity.

Laser wavelength	514.5 nm
Measured half angle of beams in air	3.65°
Dimensions of the measuring volume in air:	
Major axis	2.53 mm
Minor axis	146 μm
Fringe spacing	4.041 μm
Frequency shift	0.6 MHz

When measuring inside the test cell, the horizontal velocity component could not be measured directly near the inclined wall, because one of the beams collided with the wall. In such cases the u velocity component was determined using vector composition and from measurements of the vertical velocity component and of a velocity component at an angle of 24° relative to the vertical direction. Due to optical access limitations, these velocity measurements inside the cell were not performed at the *x*–*y* the centre-plane, but at a plane ($z/W = 0.45$) closer to the side wall, but where the effect of the end wall on the flow was still negligible, as will be shown in Section 4. Typical uncertainties associated to the measurement of the mean streamwise velocity data were estimated to be ±1% increasing to 2% for the transverse mean velocity and to 3.5% for the indirectly measured mean horizontal velocities inside the cell.

3. Fluid preparation and rheology

Measurements of the flow field were carried out with two aqueous polymer solutions based on xanthan gum (XG) and polyacrylamide (PAA) and for comparison purposes a glycerol–water mixture was used as a reference Newtonian fluid. The XG (supplied by the Kelco Division of Merck) is a food-grade polymer with a high molecular weight and was studied at a weight concentration of 0.2%. The PAA (reference Separan AN-934 SH) has also a high molecular weight and was studied at a weight concentration of 0.125%. To prevent bacteriological degradation, 0.02% by weight of biocide (kathon LXE from Rhom and Hass) was added to all the polymeric solutions.

All solutions were prepared with tap water following the same procedure. In a large agitated tank the polymers were added slowly to water while being stirred, after which the mixtures were agitated for further 90 minutes. The solutions rested for 24 h to ensure complete hydration of the molecules prior to their transfer to the test rig. This was carried out after the fluid was further agitated for 30 min to ensure full homogenization. Once the rig was filled, air had to be removed through appropriate traps after several short periods of pumping. Only at the end of this process the fluid was ready for any rheological or hydrodynamic measurement, i.e., this was the reference condition for rheological characterization and the assessment of degradation. A progressive cavity pump was used to minimize the mechanical degradation (decrease in rheological properties with time not exceeding 10%) and this was monitored by periodically extracting fluid from the rig for rheological characterization. This limited the use of a batch of fluid to about 72 h of pumping for the XG solution and to about 6 h of pumping for the PAA solution, after which the fluid was discarded and a new batch prepared. During all experiments, the temperature was monitored in order to accurately determine the rheological properties.

The shear rheology of the fluids was measured in a rheometer (TA-AR 2000) implemented with a cone-plate geometry. The variation of the viscometric viscosity with the shear rate of the two solutions is plotted in Fig. 3. Viscosity models were fitted to the measured data by a least square method.

The Newtonian water-glycerin solution has a constant viscosity of 0.0425 Pa s and a density of 1184 kg/m^3. For both non-Newtonian solutions, we fitted the Carreau-Yasuda model Eq. (1)

$$\eta(\dot{\gamma}) = \eta_\infty + (\eta_0 - \eta_\infty)[1 + (\Lambda\dot{\gamma})^a]^{\frac{n-1}{a}} \quad (1)$$

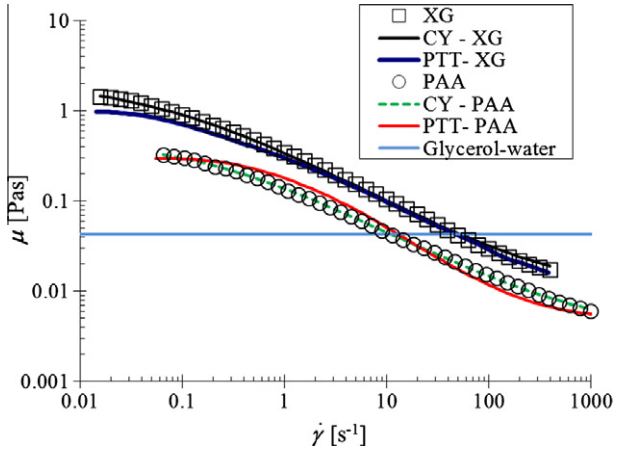

Fig. 3. Measured viscometric viscosity of PAA and XG solutions at 25 °C (symbols) and comparisons with fitted Carreau-Yasuda (CY) and PTT models (lines).

with parameters η_0, η_∞, Λ, n and a. The corresponding parameters are listed in Table 2.

We also fitted the Phan-Thien–Tanner (PTT) model with 6 modes ($\boldsymbol{\tau}_i$), where the total extra stress is given by Eq. (2).

$$\boldsymbol{\tau}_p = \sum_{i=1}^{4} \boldsymbol{\tau}_i \quad (2)$$

Each mode of the PTT model obeys the differential constitutive Eq. (3), where λ is the relaxation time, η_p is the viscosity coefficient and ξ is a coefficient accounting for the slip between the polymer molecules and the continuum medium. $\overset{\nabla}{\boldsymbol{\tau}}_i$ denotes the upper convected derivative [4] and the function $Y(tr\boldsymbol{\tau}_i) = 1 + \varepsilon\lambda tr\boldsymbol{\tau}_i/\eta_p$ depends on the trace of the stress tensor and introduces the coefficient ε, which is inversely proportional to the extensional viscosity.

$$Y(tr\boldsymbol{\tau}_p)\boldsymbol{\tau}_p + \lambda \overset{\nabla}{\underset{p}{\boldsymbol{\tau}}} + \frac{\xi}{2}\lambda\{\dot{\boldsymbol{\gamma}}\cdot\boldsymbol{\tau}_p + \boldsymbol{\tau}_p\cdot\dot{\boldsymbol{\gamma}}\} = \eta_p\dot{\boldsymbol{\gamma}} \quad (3)$$

The parameters of the adjusted PTT models are listed in Table 3 and compared with experimental data in Figs. 3–5. The adjustment of the PTT model was based on the measurements of shear viscosity and normal stresses in steady shear and of G' and G'' in small oscillatory shear flow (SAOS), as explained below.

In Fig. 4 the loss and storage moduli obtained in small amplitude oscillatory shear flow (SAOS) for the two solutions are plotted. The loss modulus (G'') is slightly higher than the storage modulus (G') for the XG solution, whereas for the PAA solution G′ is higher than G″, indicating that both solutions are moderately elastic, with the PAA solution more elastic than XG.

In Fig. 5 the measured first normal stress difference coefficient is plotted against the shear rate for the two solutions and compared with the predictions by the PTT model. These differ from the experimental data especially at large shear rates, but the uncertainty in the measurement of Ψ_1 is large because the solutions are not very concentrated and the normal stress difference is rather low.

The relaxation time of each fluid was determined using two methods: from measurements of G' and G'' in SAOS and using the capillary break-up rheometer. To determine the relaxation time from SAOS (λ_{SAOS}) we followed the approach described in Bird et al. [4], where

$$\lambda_{SAOS} = \lim_{\omega\to 0} \frac{G'/\omega}{G''} \quad (4)$$

This is essentially equivalent to fitting the G' and G'' rheological behavior of a fluid by a Maxwell model with N modes (where λ_k and η_k are the relaxation time and viscosity coefficient of each mode) and then determine λ_{SAOS} as

$$\lambda_{SAOS} = \sum_{k=1}^{N} \frac{\eta_k\lambda_k}{\eta_k} \quad (5)$$

This yielded values of λ_{SAOS} = 9.2 s for the XG solution and λ_{SAOS} = 13.6 s for the PAA solution.

To determine the relaxation time using the capillary break-up rheometer (Haake CaBER 1, Thermo Scientific), measurements were also conducted at 25 °C for the PAA solution, but at 15 °C for the XG solution (at 25 °C the filament breakup with XG was too fast to attain elasto-capillary thinning). Here, the liquid sample is put between two circular plates of 4 mm diameter, which are initially separated by a gap of 2 mm and 3 mm for the XG and PAA solution, respectively. Then, an axial step strain is imposed to separate the plates to the final gap of 8.4 mm and 12.2 mm, respectively for the XG and PAA solutions, and subsequently the diameter of the liquid thread $D(t)$ is monitored while it relaxes until breakup under the action of elastic and capillary forces. The

Table 2
Parameters of Carreau-Yasuda model adjusted to the non-Newtonian solutions.

Fluid	ρ (kg/m^3)	μ_0 (Pa s)	μ_∞ (Pa s)	Λ (s)	a	n	K (Pa s^n)
0.2% XG	1000	2.3242	0.00996	11.6875	0.50339	0.3454	–
0.125% PAA	1000	0.4378	0.00314	5.6179	0.7422	0.4285	–

Table 3
Parameters of the multimode Phan-Thien–Tanner model adjusted to the non-Newtonian data.

Mode	μ_k (Pa s)	λ_k (s)	ε	ξ
0.2% XG				
1	0.517	16.41	0.25	0.25
2	0.240	2.642	0.25	0.25
3	0.140	0.540	0.25	0.25
4	0.067	0.110	0.25	0.25
5	0.038	0.008	0.25	0.25
6	0.004	0.068	0.25	0.25
0.125% PAA				
1	1.15	18.0	0.25	0.2
2	0.293	3.15	0.25	0.2
3	0.096	0.737	0.25	0.2
4	0.031	0.168	0.25	0.2
5	0.011	0.039	0.25	0.2
6	0.010	0.006	0.25	0.2

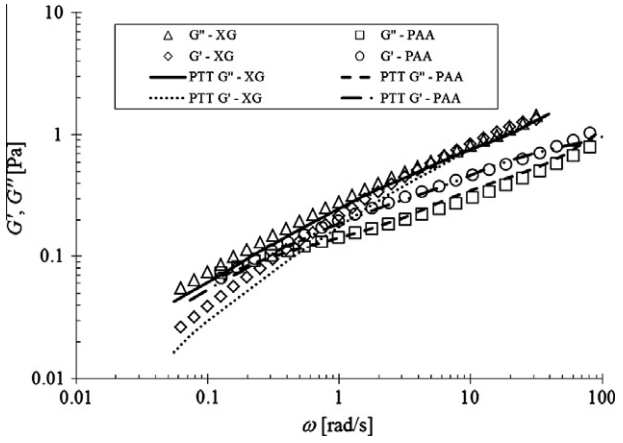

Fig. 4. Loss (G'') and storage (G') moduli for the PAA and XG polymer solutions at 25 °C (symbols) and comparison with fitted PTT models (lines).

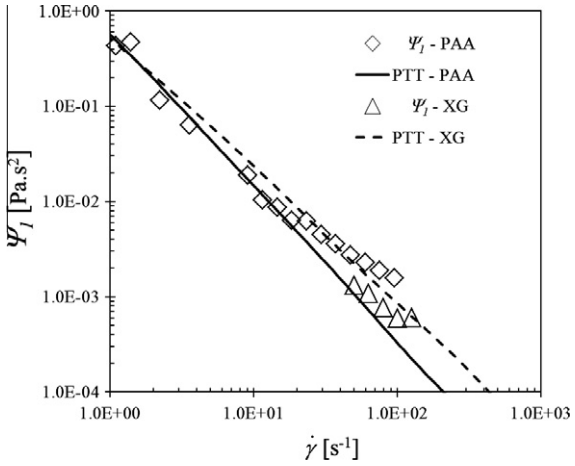

Fig. 5. Variation of the first normal stress difference with the shear rate for the XG and PAA solutions at 25 °C (symbols) and comparison with fitted PTT models (lines).

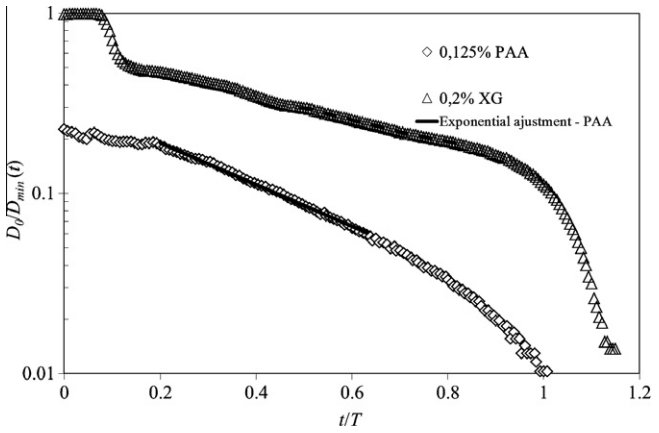

Fig. 6. Exponential decay of filament diameter during a CaBER experiment for PAA at 25 °C and XG at 15 °C.

relaxation time is determined from the fitting to the experimental decay of $\log[D(t)]$ versus t in the elasto-capillary thinning regime and yielded a value of $\lambda_{CaBER} = 10$ ms for the XG solution and of $\lambda_{CaBER} = 40$ ms for the PAA solution. Fig. 6 show the corresponding diameter decays and fittings for the XG and PAA solutions. Using the time-temperature superposition principle, the relaxation time determined at 15 °C for the XG solution was converted to the working temperature (cf. [26] noting the mistake there with the application of the principle to the relaxation time).

On a final note we would like to point out that fluid rheology, and in particular the relaxation time and other elastic properties, are very sensitive to the protocol for manufacturing the fluids. In this case, for which large volumes of fluid must be prepared, it is also necessary to pump fluid around the rig to guarantee homogenization and the removal of air bubbles that impairs optical measurements. This pumping degrades the fluid and decreases the magnitude of the material properties to values which are lower than for fresh samples or for fluids made in small amounts using low speed magnetic stirrers (as when preparing samples for microfluidics).

4. Experimental flow results

4.1. Fully-developed flow in the rectangular duct

Transverse profiles of streamwise velocity were measured along the rectangular duct and compared with theoretical expressions for fully-developed flow. The Reynolds number used, Re^* in Eq. (6), was defined by Kozicki et al. [17]. The generalized Kozicki Reynolds number is based on the mean inlet velocity, U, measured by the flowmeter, and the length scale is the hydraulic diameter of the rectangular channel. Parameters a and b take on the following values: $a = 0.4311$ and $b = 0.9281$ for an aspect ratio of 13.

$$Re^* = \frac{\rho (U)^{2-n} D_H^n}{8^{n-1} k \left(b + \frac{a}{n}\right)^n} \tag{6}$$

The Weissenberg number, Wi, is also calculated on the basis of the hydraulic diameter and the bulk velocity in the inlet

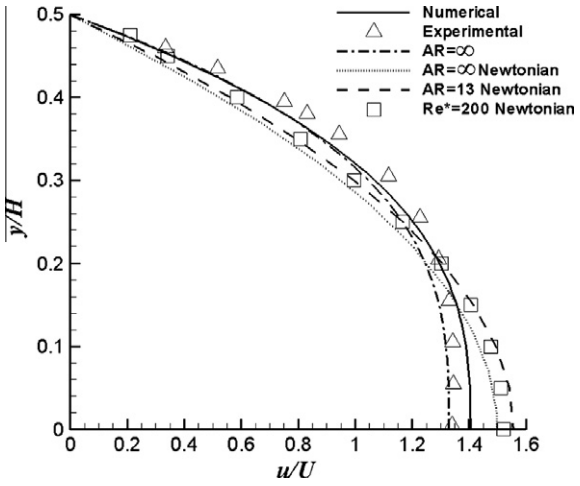

Fig. 7. Streamwise velocity profile at $x/H = -5.7$ for aqueous solution of 0.2% XG at $Re^* = 200$ and $Wi = 0.092$: comparison between measurements (symbols) and theoretical data (lines).

rectangular duct as in Eq. (7). The relaxation time used is that determined in the CaBER measurements.

$$Wi = \frac{\lambda_{CaBER} U}{D_H} \tag{7}$$

The velocity data are, from now on, normalized by the bulk velocity at the rectangular channel (U), the x and y coordinates are normalized by the height of the inlet duct (H) and the z coordinate by the half-width of the channel (W).

In Figs. 7 and 8, the measured profiles for the XG and PAA solutions, both for $Re^* = 200$ in the fully developed region ($x/H = -5.7$), are compared with the theoretical data for the corresponding parallel plate flow ($AR = \infty$), respectively. The corresponding Wi are 0.092 and 0.22 for the flows of XG and PAA solutions. The plot includes experimental data for a Newtonian fluid at the same Kozicki Reynolds number as well as the corresponding analytical profiles for $AR = \infty$ and $AR = 13$. Across most of the channel the Newtonian data lies on the $AR = 13$ curve except near the centre plane where it lies between the two analytical solutions and at 2.5% away from the $AR = 13$ profile. The data for the PAA solution lies on the theoretical curves meanwhile for the XG solution there

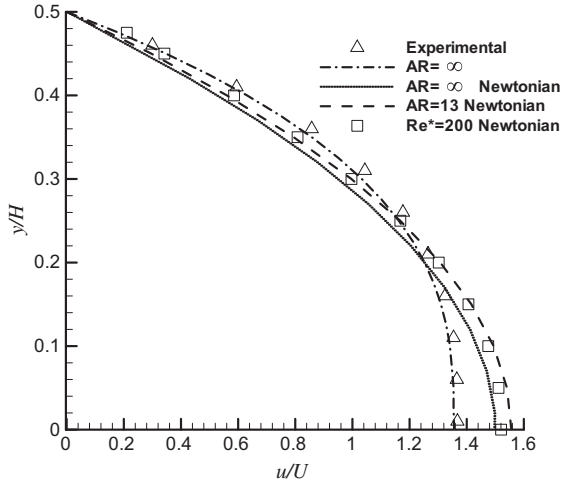

Fig. 8. Streamwise velocity profile at $x/H = -5.7$ for aqueous solution of 0.125% PAA at $Re^* = 200$: and $Wi = 0.22$: comparison between measurements (symbols) and theoretical data (lines).

is a difference of 2% well within experimental uncertainty. Fig. 7 also includes the predicted velocity profile for a purely viscous Generalized Newtonian fluid represented by the Carreau-Yasuda fitting to the 0.2% XG solution and the difference in relation to the measured data is also of the order of 2%, but with the opposite sign.

Velocity profiles were also measured from one end wall to the other end wall to check for symmetry relative to the x–y centre-plane. For all flow cases the profiles were shown to be symmetric, but the corresponding figures are not shown for compactness. Additionally, it was found that the presence of the end walls is not felt in the bulk of the flow, between $z/W = \pm 0.6$ for XG solution and $z/W = \pm 0.5$ for PAA solution.

For the non-Newtonian solutions the velocities in the center of the duct, are lower than those for the Newtonian solutions, because of the shear-thinning behaviour of the non-Newtonian solutions.

4.2. Approach flow and impinging flow region

The progression of the streamwise velocity at the end of the rectangular duct and in the impinging jet region is shown in Figs. 9 and 10 along the x-y centre-plane for the XG and PAA solutions, respectively. Figs. 9 and 10 include data for a Newtonian fluid at the same Reynolds number, $Re^* = 200$. The first profile, at $x/H = -5.7$, corresponds to the fully-developed flow inside the channel. At $x/H = -0.4$ the effect of the plate is still rather weak, with values of velocity differing from the fully-developed profile by less than 2.5%. For the non-Newtonian solutions, this difference is higher, especially for the PAA solution. The decrease of velocity near the centreline and the flow acceleration near the walls are clearly seen as the fluid approaches the plate, especially after the fluid exits the rectangular duct, i.e., when there is a large drop in u-velocity in the center and the no-slip condition ceases to apply because the upper and lower walls are absent. These measurements were carried out from the top to the bottom wall and showed symmetry relative to the x–z centre-plane for all cases; these are not shown for compactness. As happens in the entrance duct, at the same position, the velocities at the center are higher for the Newtonian case and this is again related to the shear-thinning behavior of the non-Newtonian solutions used.

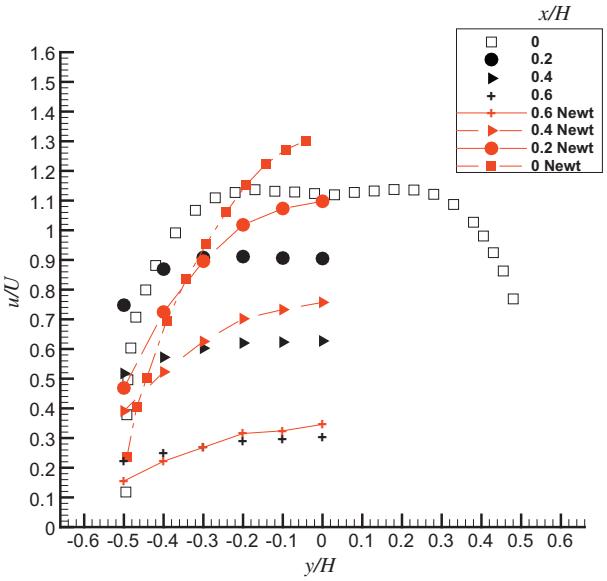

Fig. 9. Transverse profiles of streamwise velocity for 0.2% XG (symbols) and Newtonian (symbols with lines) solutions at the end of the duct and in the impact region for $Re^* = 200$.

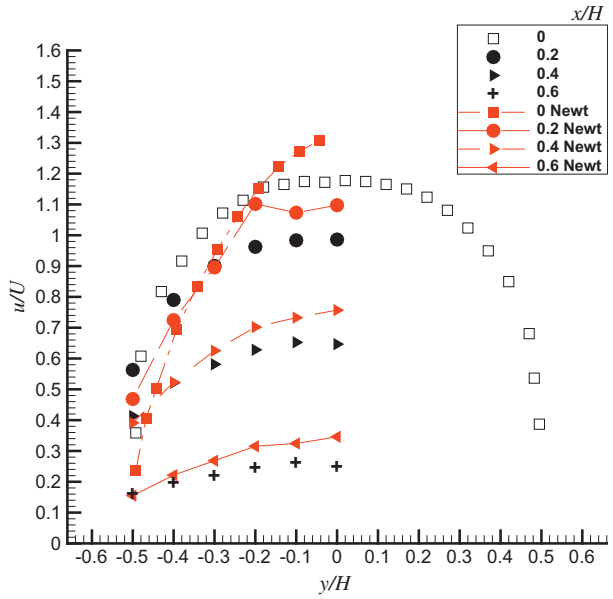

Fig. 10. Transverse profiles of the streamwise velocity for the 0.125% PAA (symbols) and Newtonian (symbols with lines) solutions at the end of the duct and in the impact region for $Re^* = 200$.

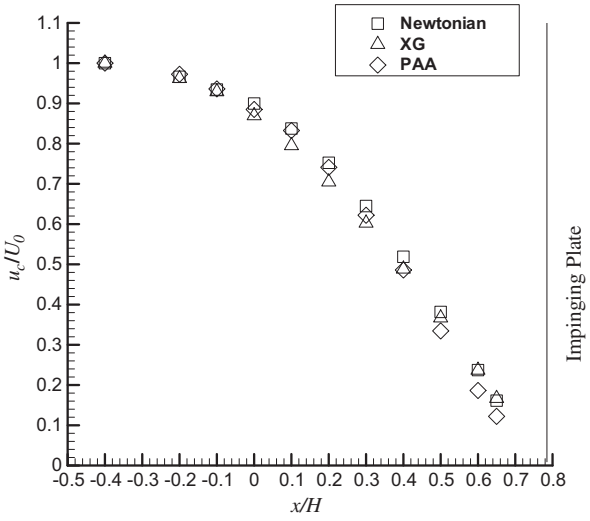

Fig. 11. Streamwise profile of the on-axis streamwise velocity in the approach region for $Re^* = 200$ at $z/W = 0$.

Figs. 9 and 10 also show symmetry relative to x–z centre-plane. As happens in the entrance duct, at the same position, the velocities at the center are higher for the Newtonian case and this is again related to the shear-thinning behavior of the non-Newtonian solutions used.

Fig. 11 represents the streamwise evolution of the streamwise velocity along the central axis (u_c) in the region $-0.4 \leqslant x/H \leqslant 0.8$, i.e., at the end of the rectangular duct ($x < 0$) as well as in the impinging region above the plate ($x > 0$) and also the corresponding profile for Newtonian fluids. The velocity has been normalised by the corresponding fully-developed centreline velocity at $z/W = 0$ in the duct (U_0). The decrease of u_c/U_0 is of only about 10% inside the duct and the strong flow deceleration is seen in the vicinity of the impinging plate ($0.2 \leqslant x/H \leqslant 0.8$). Even though the flow is essentially controlled by inertia, we can see that the velocity reduction is slightly higher in the impinging zone ($x/H > 0.4$) for the PAA solution comparatively to the XG solution and to the

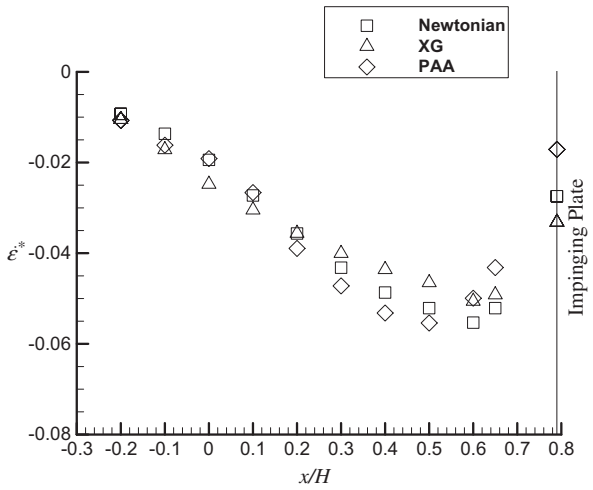

Fig. 12. Variation of the velocity profile of the longitudinal component (u) in the symmetry plane, $z/W = 0$, for $Re^* = 200$.

Newtonian fluid. This is so because the PAA flow is more elastic than the other fluids and consequently the developed normal stresses, and its corresponding streamwise gradients, are higher than for the other fluids. Therefore, the PAA solution will start to deviate earlier from the plate than the Newtonian and XG solutions.

From the measured velocity data we also calculated the normal gradient of the streamwise velocity, which is plotted in Fig. 12 in the following dimensionless form.

$$\dot{\varepsilon}^* = \frac{\partial u}{\partial x}\frac{D_H}{U_0} \tag{8}$$

Similarly, Fig. 13 plots for all flows the dimensionless streamwise advective acceleration as in Eq. (9).

$$a^* = u\frac{\partial u}{\partial x}\frac{D_H}{U_0^2} \tag{9}$$

The dimensionless normal gradient of the streamwise velocity is now higher for the PAA solution than for the XG and Newtonian solutions, for $0.2 \leqslant x/H \leqslant 0.5$, with the peak value at $x/H = 0.5$,

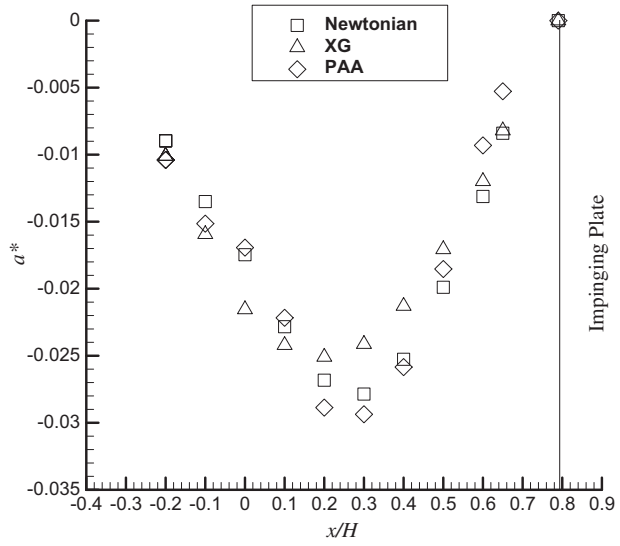

Fig. 13. Acceleration profile in the symmetry plane, $z/W = 0$, for $Re^* = 200$.

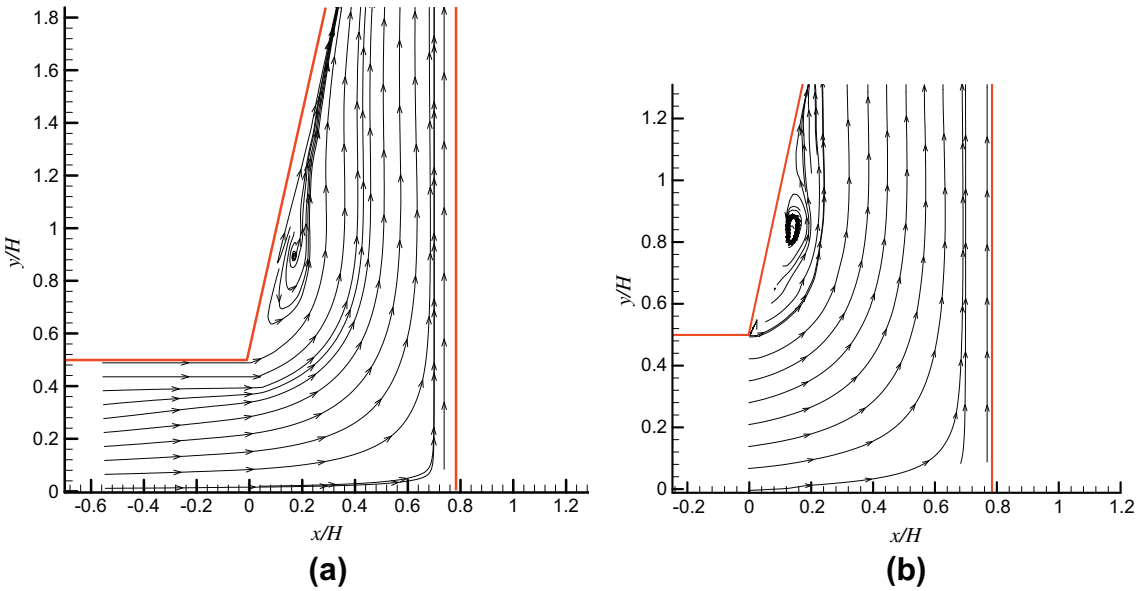

Fig. 14. Flow patterns inside the cell; streamlines contour plots of u and v velocity components at $z/W = 0.45$; (a) 0.2% XG at $Re^* = 200$ and $Wi = 0.092$; (b) 0.125% PAA at $Re^* = 200$ and $Wi = 0.22$.

whereas for the other solution it occurs at $x/H = 0.6$, i.e. there is an advance of the peak of the nondimensional variation of the streamwise velocity.

The acceleration is negative, meaning deceleration, and the region of strongest deceleration is between $0 \leqslant x/H \leqslant 0.5$. As the fluid further approaches the plate, the deceleration drops to zero since the plate is impermeable (cf. Fig. 13). Note that due to blockage of the laser beams by the solid walls, we could not measure close to the impinging plate. The peak of the deceleration occurs for the PAA and Newtonian solution at $x/H = 0.3$ and the highest value occurs for the PAA solution. Nevertheless, as we approach the impinging plate the deceleration of the PAA solution is less intense than that observed for the other fluids. This behavior agrees with the previous observation of a higher effect of elasticity over the deceleration still in the interior of the duct. Note that the PAA solution is composed by flexible molecules, while the XG solution is composed by semi-rigid molecules.

4.3. Flow within the cell

The flow symmetry inside the test cell, relative to the x–z centre-plane, was assessed for all flows by performing measurements of the streamwise velocity at symmetric y/H planes in the 4 mm thick outlet channels. These provided profiles of v at $y/H = +4.9$ (upper channel) and $-v$ at $y/H = -4.9$ (lower channel), which compared well for all flows within the experimental uncertainty. These profiles were not taken at $z/W = 0$, but at $z/W = 0.45$ to avoid blockage of the laser beams by the walls. This location is inside the region $-0.6 \leqslant z/W \leqslant +0.6$, where the streamwise velocity is unaffected by the end walls, as shown in Section 4.1. For all flows, the difference between both velocity profiles is small showing that there is symmetry relative to x–z centre-plane. However, the upper and lower profiles do not collapse as well as in the inlet duct and impinging plate region, showing in one case some deviations, which we attribute to a less successful positioning of the impinging

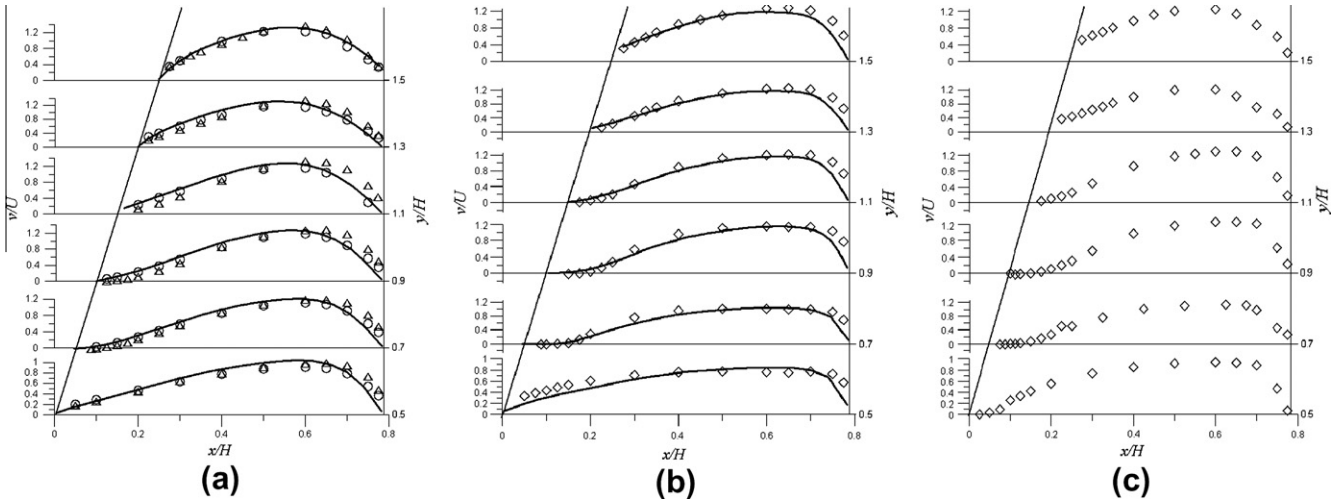

Fig. 15. Vertical velocity profiles at $z/W = 0.45$ in the cell (a) Newtonian, O $Re^* = 100$ and $\Delta Re^* = 200$; (b) 0.2% XG at $Re^* = 200$ and $Wi = 0.092$; (c) 0.125% PAA at $Re^* = 200$ and $Wi = 0.22$. Symbols correspond to experimental data and lines pertain to the corresponding numerical predictions for the Newtonian solution at $Re^* = 200$ (a) and for the Carreau-Yasuda model fit to the 0.2% XG solution (b).

plate to set the 4 mm channel thickness. This is achieved by four screws with the help of spacers, which need to be removed prior to the final screw tightening, leading to an estimated uncertainty that could be as much as 150 μm from the intended 4 mm separation, which by itself represents already ±3.8% of the channel thickness on each side (upper and lower outlet channels). It is also important to refer that the flow visualizations did not show signs of top-bottom flow asymmetry.

In all flows, two recirculation zones were observed near the inclined plane walls, one near each wall as shown in the streamline plots of Fig. 14. There the flow inside the cell refers to the upper side, with Fig. 14a and b for XG and PAA, respectively. These streamlines were produced as stream-traces by Tecplot from the input of experimental v and u velocity data (2D data) at the various measured planes. To draw the stream-traces, Tecplot produces additional velocity data points by interpolation based on the experimental data and the additional input of a zero velocity at the sloping and flat walls.

In Fig. 15, profiles of the measured (symbols) and computed (lines) vertical velocity component inside the cell are shown for Newtonian and non-Newtonian fluids in the laminar regime. Fig. 15a plots Newtonian profiles for $Re^* = 100$ and $Re^* = 200$; for $Re^* = 100$ there is no flow separation whereas for $Re^* = 200$ the normalized length of the recirculation zone is $L_R/H = 0.25$. Fig. 15b and c plot the non-Newtonian results for the XG and PAA solutions at $Re^* = 200$, respectively. The lengths of the recirculation are $L_R/H = 0.35$ and $L_R/H = 0.30$ for the XG and PAA solutions respectively, showing that the non-Newtonian behavior enhances the extension of separated flow region. Note that the negative velocities in the separated flow region are very small compared with the main stream flow (of the order of 0.001 of U), but nevertheless there is a separated flow region as is also shown in the Newtonian flow visualization of Fig. 16. The experimental data for L_R were determined from the detailed velocity measurements by LDA of the velocity component parallel to the inclined wall using a fine mesh of points (the points closest to the wall were at 0.5 mm from the wall). This provided a "streamwise" profile of the "streamwise" velocity component ("streamwise" here in the sense of parallel to the inclined wall) having negative velocities in regions inside the separated flow region and positive velocities after reattachment. L_R was determined from an interpolation to zero velocity in this profile. It should also be mentioned that the "streamwise" positive and negative velocities in this region were extremely small.

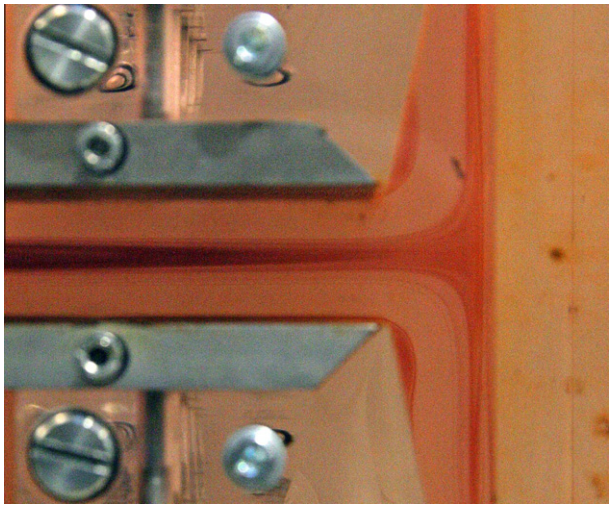

Fig. 16. Flow visualization with glycerol–water at $Re^* = 200$.

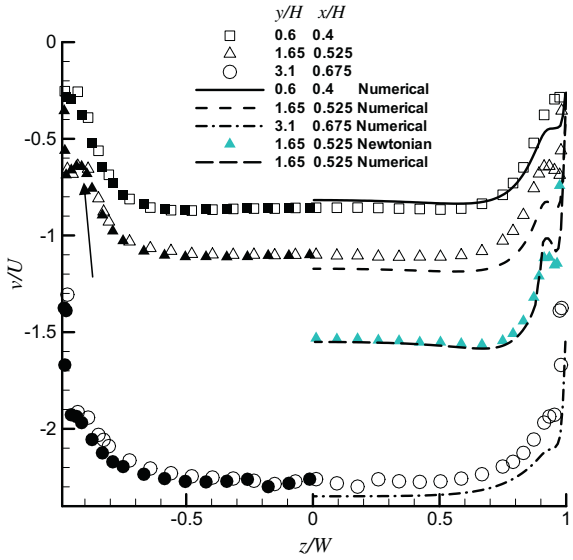

Fig. 17. Spanwise profiles of the streamwise velocity at various locations for 0.2% XG at $Re^* = 200$ and $Wi = 0.092$ to illustrate the three dimensional flow effect near the side walls. Closed black symbols refer to the reflected profiles, blue symbols are for a Newtonian solution at the same Reynolds number and lines pertain to the purely viscous numerical solution for the Carreau-Yasuda viscosity model fit to the 0.2% XG solution. (For interpretation of the references to colour in this figure legend, the reader is referred to the web version of this article.)

Fig. 15a and b include also velocity profiles obtained from the purely viscous 3D numerical predictions explained in Section 5 (Newtonian model (a) and Carreau-Yasuda (b) model of Fig. 3, respectively). The comparison is reasonable, but computed velocities slightly over predict the measurements near the inclined plate and under predict them near the impinging plate.

The Newtonian flow visualization picture in Fig. 16 also shows the growth of the boundary layers by the wall jets along the impinging plate.

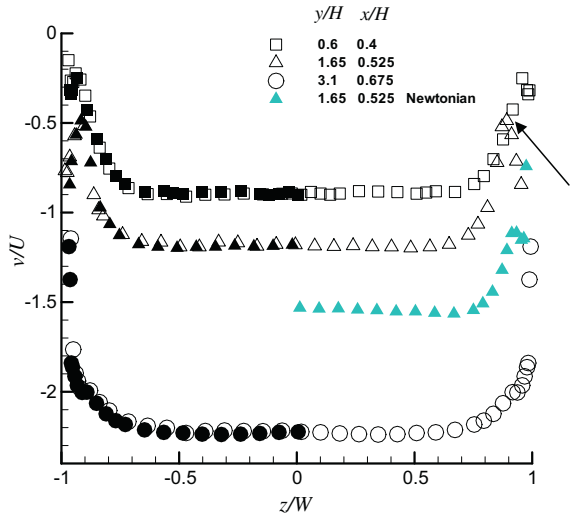

Fig. 18. Spanwise profiles of the streamwise velocity at various locations for 0.125% PAA at $Re^* = 200$ and $Wi = 0.22$ to illustrate the three dimensional flow effect near the side walls. Closed black symbols refer to the reflected profiles, blue symbols are for a Newtonian solution at the same Reynolds number. (For interpretation of the references to colour in this figure legend, the reader is referred to the web version of this article.)

4.4. Three dimensional effect

The complexity of the flow inside the cell, and the effect of the flat side walls combine to create a characteristic three-dimensional effect near these flat walls, which eliminates the separated flow regions there, as previously found for Newtonian fluids [5]. This three dimensional flow feature was visualized and is shown and discussed in this section.

Some spanwise profiles of the vertical mean velocity measured inside the cell are plotted in Figs. 17 and 18 for the solutions of XG and PAA, respectively. They exhibit negative velocities since they were measured in the lower half of the cell test section. The profiles show that local maxima and minima in the vertical velocity are stronger near the sloping wall and at the beginning of the narrowing cell than elsewhere. Simultaneously, no separated flow regions are seen to exist near the flat side walls. Flow visualizations with a dye injection technique and especially with small tracer bubbles have shown the existence of a helical flow motion near the inclined wall. Fluid particles entering the separated flow region rotate away from the center and flow towards the side walls. Before reaching these end walls, the fluid particles in helical motion exit the separated flow region, which vanishes, and merge with the main flow nearer to the inclined plate. Further away from the inclined wall, the main flow near the flat side wall is actually swirling as will be shown by the numerical results in Section 5.3. Since the swirl velocities are much smaller than the streamwise velocities we could not see it in the flow visualizations, but it is the combination of these effects that create the near wall peaks seen in Figs. 17 and 18. In Fig. 17, for the XG solution, these near wall peaks are observed at $z/W \approx \pm 0.9$ for $y/H = 1.65$, $x/H = 0.525$, just downstream of the separated flow (these are indicated by arrows in the figures) and they were confirmed by the numerical calculations for the Newtonian fluid and the purely viscous Carreau-Yasuda model fit to the viscosity of the 0.2% XG solution also plotted, hence these are not due to viscoelasticity. Further downstream, along the converging channel, the velocities rise due to continuity, but there are still traces of a perturbation in the velocity profiles taken at $z/W \approx \pm 0.95$ for $y/H = 3.1$, and $x/H = 0.675$ (c.f. Fig. 17). For the PAA solution, the peak is stronger than the peak for the XG solution and they are both stronger than for the Newtonian fluid as we can see in Figs. 17 and 18. Therefore, the experiments suggest that non-Newtonian behavior enhances these effects and consequently the near wall jet. The closed symbols are the reflection of the velocity profile on one side of the duct onto the other half showing that there is symmetry relative to x–y centre-plane. These flow features will be confirmed and in the numerical simulations of section 5.

5. Numerical results

5.1. Governing equations

The basic equations solved are those for 3-D, incompressible and isothermal laminar flow for constant density purely viscous generalized Newtonian fluids, where the viscosity only depends on the second invariant of the strain-rate tensor (S_{ij}). In Cartesian index notation, the governing equations are the continuity equation:

$$\frac{\partial u_i}{\partial x_i} = 0 \tag{10}$$

and the equation of linear momentum :

$$\frac{\partial \rho u_i}{\partial t} + \frac{\partial \rho u_j u_i}{\partial x_j} = -\frac{\partial p}{\partial x_i} + \frac{\partial \tau_{ij}}{\partial x_j} \tag{11}$$

where u_i is the velocity component along the Cartesian coordinate x_i, ρ the fluid density, p the pressure and τ_{ij} the extra stress tensor. These equations allow the determination of the velocity and pressure flow fields. A fully-implicit finite-volume method is used to solve Eqs. (10) and (11). The in-house numerical code allows the use of a number of different constitutive equations for viscoelastic and purely viscous generalized Newtonian fluids and has been extensively validated and documented in the literature [2,3,8]. The latter is the case in this work and the Generalized Newtonian fluid model of Eq. (12) is used, where the viscosity function is given by the power-law model (Eq. (1)), and the scalar shear rate ($\dot{\gamma}$) is defined on the basis of the second invariant of the strain-rate tensor $\dot{\gamma} \equiv \sqrt{2S_{ij}S_{ij}}$ with $S_{ij} = (\partial u_i/\partial x_j + \partial u_j/\partial x_i)/2$.

$$\tau_{ij} = \eta(\dot{\gamma})\left[\frac{\partial u_i}{\partial x_j} + \frac{\partial u_j}{\partial x_i} - \frac{2}{3}\frac{\partial u_k}{\partial x_k}\delta_{ij}\right] \tag{12}$$

For validation purposes numerical predictions are compared with experimental data for Newtonian and the non-Newtonian xanthan gum solution at $Re^* = 200$ (and $Wi = 0.092$ for the XG solution). For both polymer solutions viscoelastic calculations were attempted using the Phan-Thien—Tanner rheological constitutive equation [25] fit to the rheology of the fluids, but unfortunately none of these 3D viscoelastic simulations converged in this flow, even when using such techniques as the matrix-logarithm of the conformation tensor [14], which was implemented in our finite volume code by Afonso et al. [1]. For these reasons we limit the comparison to calculations for the purely viscous Generalized Newtonian model and to the xanthan gum solution, which is significantly less elastic than the PAA solution. Since the xanthan

Table 4
Grid information.

Grid	Block1			Block2			
	N_x/f_x	N_y/f_y	N_z/f_z	N_x/f_x	N_y/f_y	N_z/f_z	
M15	50/0.8926	15/1	15/1.0494	20/1	15/1	15/1.0494	
M20	67/0.9183	20/1	20/1.03683	26/1	20/1	20/1.03683	
M20 a)	67/0.9183	20/1	120/1.0061	26/1	20/1	120/1.0061	
M30	100/0.9448	30/1	30/1.0244	39/1	30/1	30/1.0244	
M30 a)	100/0.9448	30/1	60/1.01213	39/1	30/1	60/1.01213	
M30 b)	100/0.9448	30/1	70/1.0104	39/1	30/1	70/1.0104	
M40	133/0.9583	40/1	40/1.0183	52/1	40/1	40/1.0183	
	Block3			Block4			No. of total cells
M15	20/1	88/1.0005	15/1.0494	20/1	38/1.0736	15/1.0494	53,550
M20	26/1	117/1.0004	20/1.03683	26/1	50/1.0547	20/1.03683	124,040
M20 a)	26/1	117/1.0004	120/1.0061	26/1	50/1.0547	120/1.0061	744,240
M30	39/1	175/1.0003	30/1.0244	39/1	75/1.0003	30/1.0244	417,600
M30 a)	39/1	175/1.0003	60/1.11213	39/1	75/1.0003	60/1.01213	835,200
M30 b)	39/1	175/1.0003	70/1.0104	39/1	75/1.0003	70/1.0104	974,400
M40	52/1	233/1.00020	40/1.01825	52/1	100/1.01825	40/1.01825	988,640

gum is made from semi-rigid molecules [18] the elasticity of its solutions is felt more sensibly in flows with small deformation than in flows with large deformations as in this case [29]. Hence its approximation by a purely viscous model is reasonable as will be shown. Nevertheless, this xanthan gum solution can still exhibit dramatic elastic effects as in turbulent pipe flow, as demonstrated by Escudier et al. [9].

5.2. Numerical procedure and validation

The numerical method is briefly outlined below as it has been described in detail in Oliveira [22]. The numerical simulations were carried out with a finite-volume method using non-orthogonal collocated grids and second order accurate differencing schemes to discretize all terms of the transport equations [23,24]. The main code is interfaced with a mesh generation pre-processor and adequate data post-processor, as described in Oliveira [22]. The basic differencing schemes were central differences for the diffusion terms and a high-resolution method, CUBISTA described in Alves et al. [2,3], for the convective terms. The solution algorithm was a modified version of the SIMPLEC algorithm of Van Doormal and Raithby [28] adapted for time marching as explained in Issa and Oliveira [15], where details to evaluate mass fluxes at cell faces are given.

Symmetry in terms of planes x–y and plane x–z was considered (Fig. 2b), based on the experimental work presented in previous sections and on preliminary numerical tests done to assess the adequacy of the computational domain. Therefore, the numerical domain adopted is just a quarter of the physical domain. Symmetry conditions were assumed on the two symmetry center planes, and at the wall, all the velocity components were set to zero. At the inlet of the rectangular duct, the flow profile was set to uniform.

The computational grids were generated using patched blocks, one for the inlet of the channel, two for the cell zone, and one for the outlet of the channel. A schematic representation of the blocks used in the numerical simulations is shown in Fig. 2b and details of the mesh are given in Table 4, listing the number of internal cells in the three directions (N_x, N_y, N_z) and the corresponding geometric expansion (or contraction) factors for mesh spacing (f_x, f_y, f_z). The mesh spacing was non-uniform, with control volumes concentrated in the test cell zone. The expansion factors used were carefully chosen to guarantee a smooth variation in the whole domain, in particular at the interfaces between the mesh-generating blocks. Several tests with different grids were initially performed to assess the adequate size of the discrete domain as well as the degree of grid refinement required for grid-independent results.

In the grid tests, we analyze the behavior of the length (L_R) of the separated regions attached to the sloped walls (c.f. Fig. 2b). This recirculation length varies along the spanwise direction and Fig. 19 shows its variation for different meshes for $n = 1$ (Newtonian fluid) at a Reynolds number of the rectangular duct flow of $Re^* = 200$. Grid M40 is the finest, leading to just under 4 million degrees of freedom, a large computational cost. Consequently, most simulations were carried out using grid M30 a). Even though, there is a 5% difference in the length of the recirculation at the symmetry plane $z/W = 0$, relative to the value predicted by grid M40, the computational cost is not too high and hence its selection for the remaining numerical investigation. Note also that the used grid M30 a) is actually finer than grid M40 in the spanwise direction in order to better resolve variations along z.

For these purely viscous calculations the viscosity of the XG solution was fitted with the Carreau-Yasuda model (Eq. (2)), which

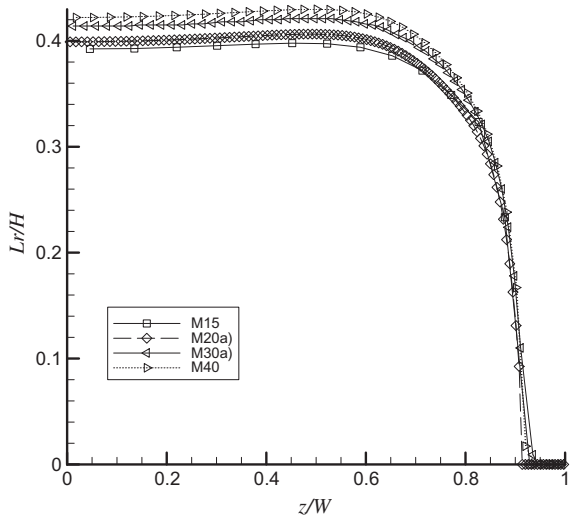

Fig. 19. Recirculation length, for $Re^* = 200$ (Newtonian fluid), along z dimension for several meshes.

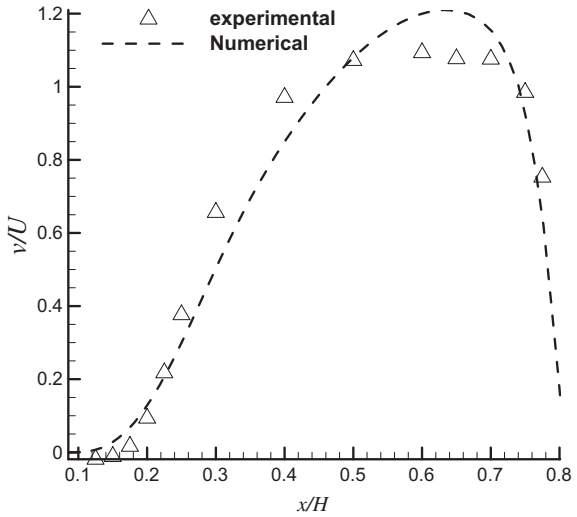

Fig. 20. Transverse profiles of streamwise velocity in the cell at $y/H = 0.8$, $z/W = 0.45$ for the 0.2% XG solution at $Re^* = 200$: experiments (symbols) and numerical (line).

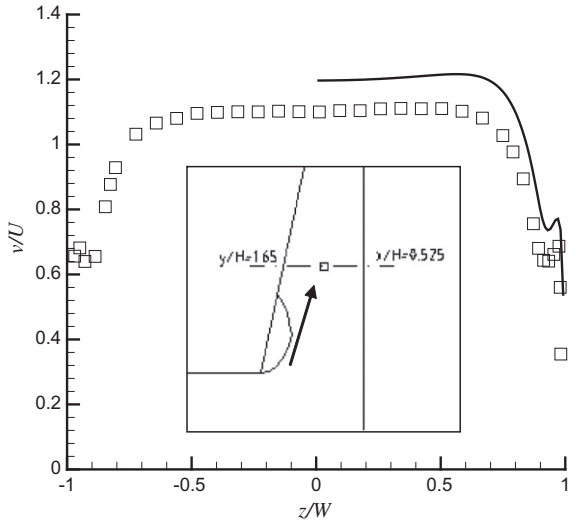

Fig. 21. Spanwise profile of streamwise velocity within the cell for 0.2% XG at $Re^* = 200$ at $y/H = 1.65$, $x/H = 0.525$ (see also inset): experiments (symbols) and numerical (line).

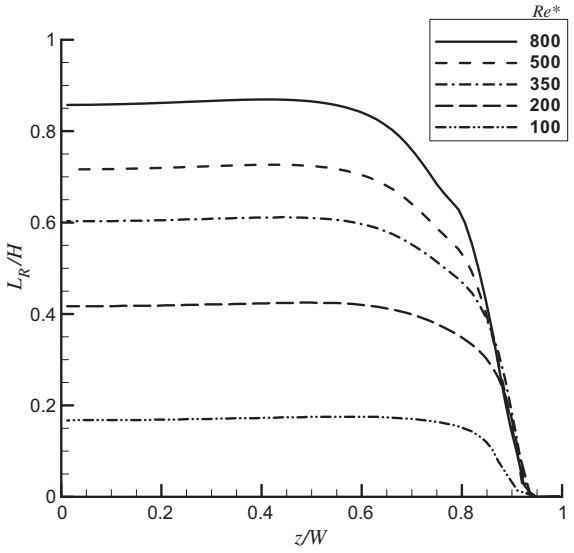

Fig. 22. Recirculation length (L_R) versus Re^* along the spanwise direction for a distance $h = 4$ mm and $n = 1$ (Newtonian behavior).

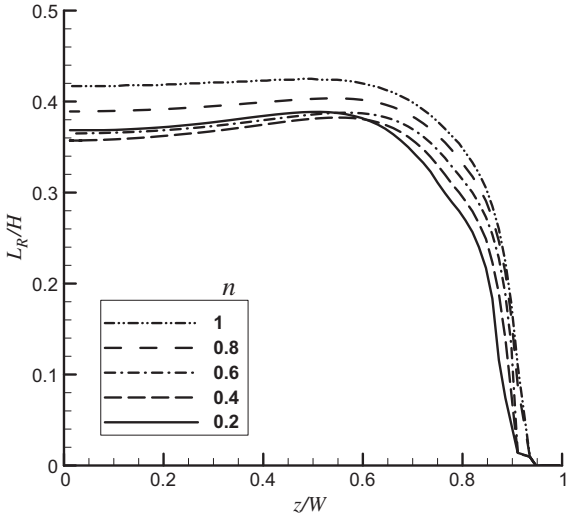

Fig. 23. Spanwise variation of the recirculation length with shear-thinning (n) for $Re^* = 200$.

had the rheological parameters listed in Table 2. The validation is carried out with three sets of data:

(1) Predicted transverse profiles of streamwise velocity along the rectangular duct are compared with analytical solutions for fully-developed flow pertaining to $AR = \infty$ and with experimental data. This comparison is shown in Fig. 7 and is aimed to ensure that the flow is completely fully-developed well upstream the inlet of the cell. The differences observed are within experimental uncertainty;
(2) Transverse profiles of streamwise velocity within the cell shown in Fig. 15 (again the comparison is quite good even for the 0.2% XG fluid) and below in Fig. 20;
(3) Spanwise profiles of streamwise velocity within the cell in Fig. 21.

In Fig. 20 the experimental transverse profiles of the streamwise velocity at $y/H = 0.8$ and $z/W = 0.45$ are represented and compared with the results from the numerical simulation for $Re^* = 200$.

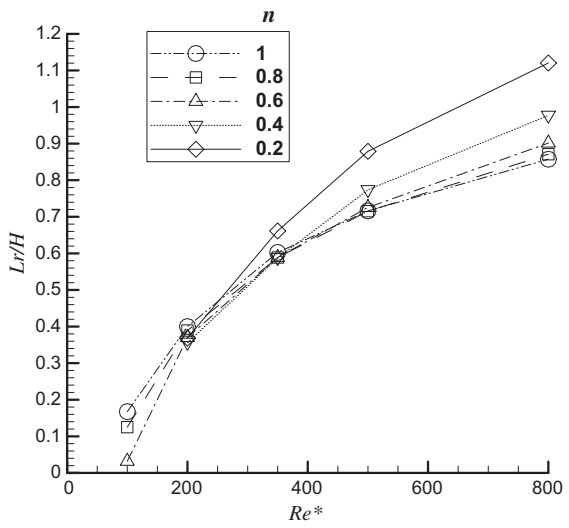

Fig. 24. Variation of the recirculation length at the $z/W = 0$ centre plane with Re^* and n.

Here, the flow is no longer fully-developed and there is no analytical solution. As we can see, there is a fairly good agreement between the numerical and experimental data. The differences between predictions and experiments for the 0.2% XG solution are larger than for the Newtonian case (not shown here for conciseness), but it must be reminded that the XG solution is sufficiently viscoelastic to affect the mean flow [7], whereas here only the viscous behavior is captured by the adopted constitutive equation. The fluid elasticity generates an imbalance of the normal stresses, which will create a secondary flow in the fully-developed rectangular duct flow, leading to changes in the streamwise velocity. The secondary flow is weak and we could not measure it in the rectangular duct, but it could explain the observed differences in the shape of the streamwise velocity profile. A better prediction will need to be carried out in the future using an adequate constitutive equation to model the elastic properties of this solution.

Inside the cell, a spanwise profile of streamwise velocity at $y/H = 1.65$ $x/H = 0.525$ is represented in Fig. 21 and we can see that the predicted and measured velocity profiles have the same shape, in spite of a difference of about 8%. It is also important to remark that the calculations were able to reproduce the small oscillation near the wall as seen in the experiments.

The effects of inertia and shear-thinning on the recirculation length are numerically investigated next.

5.3. Recirculation length and three-dimensional effect

The numerical results in this section are from a parametric investigation carried out exclusively with the Generalized Newtonian model with the viscosity function given by the power law in order to assess the effect of shear-thinning on the flow characteristics. Fig. 22 shows the evolution of the normalized recirculation length (L_R) along the spanwise direction (z/W) for Newtonian fluids ($n = 1$). The recirculation length is constant from the symmetry plane ($z/W = 0$) until the presence of the vertical flat walls is felt, i.e. at $z/W = 0.90$ where the recirculation bubble tends to disappear. This influence of the sidewall depends on Reynolds number, increasing with Re^*.

Fig. 23 shows the influence of the power law index n on the recirculation length at a constant Reynolds number ($Re^* = 200$). Generally, there is a small increase in L_R as the power law index n increases. The recirculation length is almost constant in the spanwise direction (z/W) for all values of n, showing a slight increase at

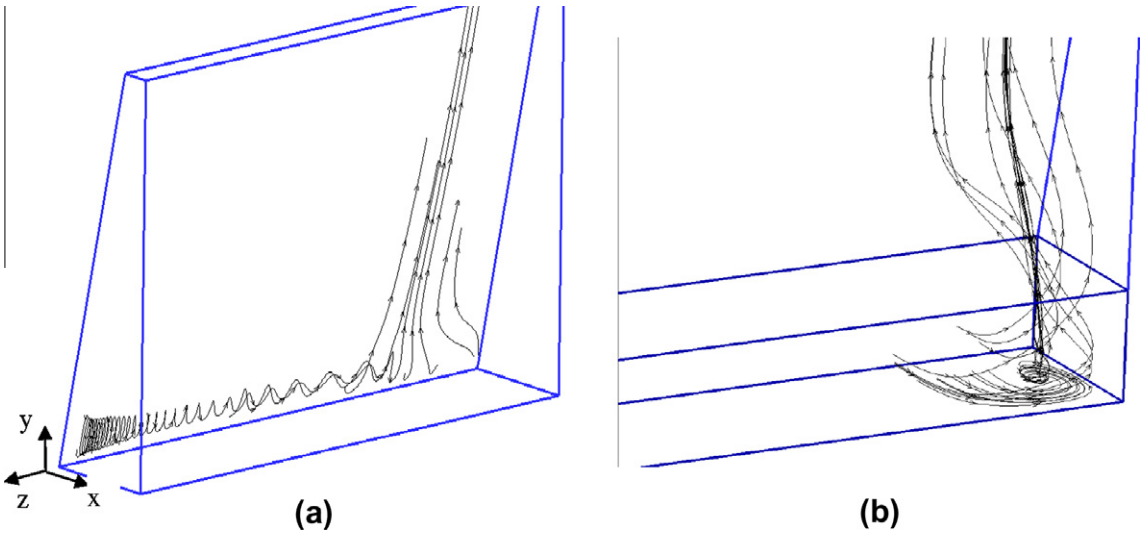

Fig. 25. Flow streaklines within the cell for $Re^* = 200$ and $n = 0.6$: (a) starting at $z/W \approx 0$ inside the separated flow region; (b) starting at the exit of the inlet duct ($x/H \approx 0$) and near the flat side wall.

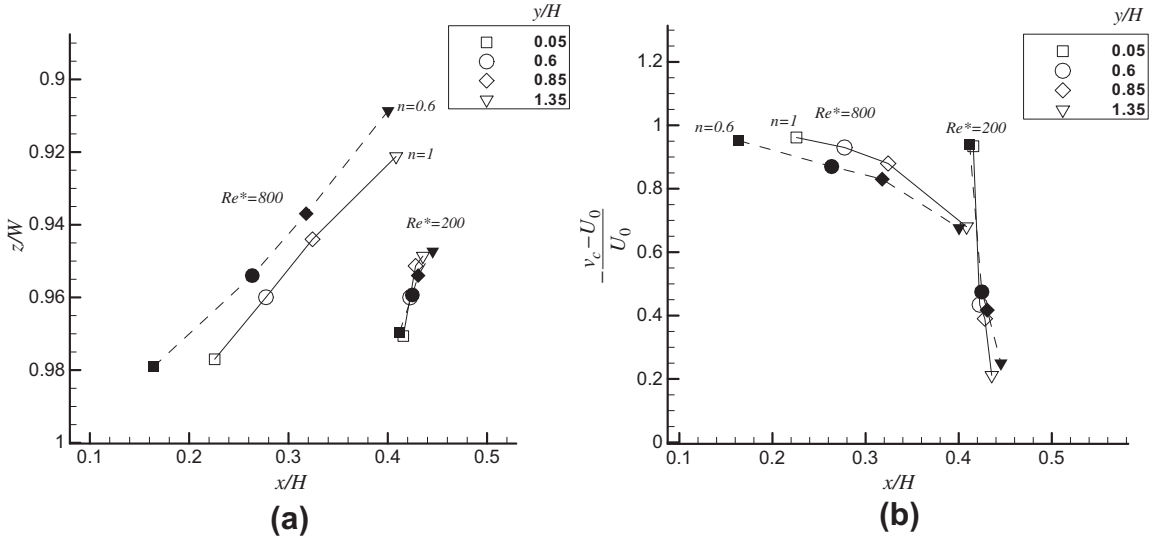

Fig. 26. Effect of Re^* and n on the side wall swirling flow: (a) location of the eye of the swirl at various planes y/H; (b) normalized streamwise velocity of the swirl axis.

the end of the central plateau and before its decrease to zero near the side wall. This effect is especially seen at low values of the power law index.

The combined influence of Re^* and n on L_R at the $z/W = 0$ centre plane is plotted in Fig. 24. It is clear that the largest effect of Reynolds number is for $n = 0.2$ due to the strong shear-thinning nature of the fluid, whereas at low Reynolds numbers the influence of n is somewhat limited. Additionally, there is a change of behavior around $Re^* = 200$: for $Re^* < 200$ the recirculation length increases for increasing values of the power index, while the reverse occurs for $Re^* > 200$.

The three-dimensional effects reported in the experiments were also observed numerically (cf. Figs. 18 and 21), which allowed a more detailed investigation. The streaklines of Fig. 25a, drawn from the purely viscous non-Newtonian predictions at $Re^* = 200$ and $n = 0.6$, show the three-dimensional flow inside the separated flow region to consist of a helical fluid motion along the spanwise direction from the centre of the cell towards the flat walls. Before reaching the flat side walls, the fluid in helical motion exits the separated flow region and joins the main flow creating a jet near the side wall, but still close to the inclined plate. Away from the inclined plate, the fluid that exits the rectangular inlet channel near the side wall turns into the vertical channel and now swirls as shown in the streakline plot of Fig. 25b. So, the oscillation in the velocity profiles seen in Figs. 17, 18 and 21 and consequent peak velocity near the flat side wall are the result of a complex interaction between the flat side wall, the flow exiting the separated flow region and the swirling motion of the fluid.

To investigate the influence of Reynolds number and shear-thinning on these three-dimensional features, the position of the swirl axis and its streamwise velocity (v_c) are shown in normalized form in Fig. 26a and b, respectively. The streamwise velocity at the center of the swirl is normalized with the bulk velocity in the inlet channel and for convenience a quantity of 1 is subtracted. The streaklines of Fig. 25b already indicated that the center of the swirl moves away from the flat side wall as the fluid moves downstream. Fig. 26a quantifies this variation showing that simultaneously the swirl center also approaches the impinging plate (x direction). This is to be expected because the channel thickness decreases as the inclined plate moves closer to the impinging plate when y/H

increases. Simultaneously, the normalized streamwise velocity at the swirl center increases (note the minus sign in Fig. 26b), as expected by continuity y.

The variation of the swirl axis position and of the magnitude of v_c along this axis are affected by shear-thinning, but especially by inertia. As inertia increases the swirl axis becomes more distorted, i.e., it varies more in both x and z directions than at lower Reynolds numbers, whereas the streamwise velocity variations become much less pronounced. Shear-thinning enhances these variations in the same direction of inertia, i.e., the position of the swirl axis varies even more on decreasing n and the variation of velocity v_c becomes even less pronounced.

6. Conclusions

The flow fields created by laminar non-Newtonian liquid jets emanating from a fully-developed rectangular duct flow and impinging on a flat plate inside a cell confined by an inclined plane wall have been studied in detail experimentally using LDA and flow visualization techniques and complemented by some numerical predictions. The flow field in the approach rectangular duct was allowed to fully-develop prior to exiting the duct and hitting the impinging plate. The flow in the bulk of the rectangular inlet duct was not influenced by the presence of the end walls due to the large aspect ratio used ($AR = 13$). Inside the inlet duct and in the cell, the flow was always symmetric in relation to the x–y and x–z centre-planes.

The study indicates the presence of a recirculation attached to the sloping wall, the size of which increased with Reynolds number. Its normalised lengths, L_R/H, are of 0.35 and 0.3 for the XG and PAA solutions, respectively and 0.35 for a Newtonian fluid at the same Reynolds number ($Re^* = 200$).

A three dimensional effect was found inside the test cell, which was characterized by a wall jet near the sidewalls, and the concomitant absence of a separated flow region there. A symmetric helical motion of separated fluid was visualized from the x–y centre-plane towards the sidewalls, confirming the characteristics measured by LDA, for the Newtonian and non-Newtonian fluids. The wall jet is stronger for the PAA solution than for the XG solution and they are both stronger than for the Newtonian fluid, showing that the non-Newtonian behaviour enhances the strength of the helical flow and the near wall jet.

The numerical predictions for the Newtonian fluid compared very well with experimental data. For the non-Newtonian fluids the predictions using a generalized Newtonian model were not as good due to the elasticity of the fluids used in the experiments. Nevertheless the differences between predictions and experiments were small, not exceeding 8%. The numerical predictions captured the 3D effects observed by flow visualization and provided physical insight. The calculations were carried out for Re^* between 100 and 800 and showed that L_R increased with Re^*, regardless the power law index, but shear-thinning made the behavior non-monotonic: at low Re^* the largest value of L_R pertained to Newtonian fluids, whereas at large Re^* the Newtonian fluids had the smallest value of L_R.

Acknowledgments

The authors acknowledge funding by FCT and FEDER via the budget of Centro de Estudos de Fenómenos de Transporte and Projects POCI56342/EQU/2004 and PTDC/EQU-FTT/70727/2004. In addition, A.S. Cavadas is grateful to FCT for the PhD grant BD/7091/2001.

References

[1] A. Afonso, P.J. Oliveira, F.T. Pinho, M.A. Alves, The log-conformation tensor approach in the finite-volume method framework, J. Non-Newt. Fluid Mech. 157 (2009) 55–65.
[2] M.A. Alves, P.J. Oliveira, F.T. Pinho, A convergent and universally bounded interpolation scheme for the treatment of advection, Int. J. Numer. Methods Fluids 47 (2003) 665–679.
[3] M.A. Alves, P.J. Oliveira, F.T. Pinho, Benchmark solutions for the flow of Oldroyd-B and PTT fluids in planar contractions, J. Non-Newt. Fluid Mech. 110 (2003) 45–75.
[4] R.B. Bird, R.C. Armstrong, O. Hassager, Dynamics of Polymeric Liquids, Fluid Mechanics, vol. 1, John Wiley and Sons, New York, 1987.
[5] A.S. Cavadas, J.B.L.M. Campos, F.T. Pinho, Flow field in impinging jets confined by slopping plane walls, in: Proceedings of 13th International Symposium on Applications of Laser Techniques to Fluid Mechanics, paper 15.5 pdf, Lisbon, Portugal, 26–29 June 2006, 2006.
[6] Q. Chen, V. Modi, Mass transfer in turbulent impinging slot jets, Int. J. Heat Mass Transfer 42 (5) (1999) 873–887.
[7] M.P. Escudier, I.W. Gouldson, A.S. Pereira, F.T. Pinho, R.J. Poole, On the reproducibility of the rheology of shear-thinning liquids, J. Non-Newt. Fluid Mech. 97 (2001) 99–124.
[8] M.P. Escudier, P.J. Oliveira, F.T. Pinho, S. Smith, Fully developed laminar flow of non-Newtonian liquids through annuli: comparison of numerical calculations with experiments, Exp. Fluids 33 (2002) 101–111.
[9] M.P. Escudier, F. Presti, S. Smith, Drag reduction in the turbulent pipe flow of polymers, J. Non-Newt. Fluid Mech. 81 (1999) 197–213.
[10] R.E. Franklin, J.M. Wallace, Absolute measurements of static-hole error using flush transducers, J. Fluid Mech. 42 (1970) 33–48.
[11] R. Gardon, J.C. Akfirat, The role of turbulence in determining the heat transfer characteristics of impinging jets, Int. J. Heat Mass Transfer 8 (1965) 1261–1272.
[12] R. Gardon, J.C. Akfirat, Heat transfer characteristics of impinging two-dimensional air jets, ASME J. Heat Transfer 65 (1966) 101–108.
[13] S.V. Garimella, R.A. Rice, Confined and submerged liquid jet impingement heat transfer, ASME J. Heat Transfer 117 (1995) 871.
[14] M.A. Hulsen, R. Fattal, R. Kupferman, Flow of viscoelastic fluids past a cylinder at high Weissenberg number: stabilized simulations using matrix logarithms, J. Non-Newt. Fluid Mech. 127 (2005) 27–39.
[15] R.I. Issa, P.J. Oliveira, Numerical predictions of phase separation in two-phase flow through T-junctions, Comput. Fluids 23 (1994) 347–372.
[16] M. Korger, F. Krizek, Mass-transfer coefficient in impingement flow from slotted nozzles, Int. J. Heat Mass Transfer 9 (1966) 337–344.
[17] W. Kozicki, C.H. Chou, C. Tiu, Non-Newtonian flow in ducts of arbitrary cross-sectional shape, Chem. Eng. Sci. 21 (1966) 665–679.
[18] R. Lapasin, S. Pricl, Rheology of Industrial Polysaccharides: Theory and Applications, Blackie Academic and Professional, 1995.
[19] J.M. Miranda, J.B.L.M. Campos, Impinging jets confined by a conical wall: laminar flow predictions, AIChE J. 45 (1999) 2273–2285.
[20] J.M. Miranda, J.B.L.M. Campos, Concentration polarization in a membrane placed under an impinging jet confined by a conical wall – a numerical approach, J. Membrane Sci. 182 (2001) 257–270.
[21] V. Narayanan, J. Seyed-Yagoobi, R.H. Page, An experimental study of fluid mechanics and heat transfer in an impinging slot jet flow, Int. J. Heat Mass Transfer 47 (2004) 1827–1845.
[22] P.J. Oliveira, Compute modeling of multidimensional multiphase flow and application to T-junctions, Ph.D. thesis, Imperial College, London, UK, 1992.
[23] S.V. Patankar, Numerical Heat Transfer and Fluid Flow, Hemisphere Publishing Company, Washington, 1980.
[24] M. Perić, A finite volume method for the prediction of three-dimensional fluid flow in complex duct, Ph.D. thesis, Imperial College, London, UK, 1985.
[25] N. Phan-Thien, R.I. Tanner, A new constitutive equation derived from network theory, J. Non-Newt. Fluid Mech. 2 (1977) 353–365.
[26] L.M. Quinzani, R.A. Armstrong, R.C. Brown, Modeling the rheology of polyisobutylene solutions, J. Rheol. 34 (1990) 705–748.
[27] R. Shaw, The influence of hole dimensions on static pressure measurements, J. Fluid Mech. 7 (1960) 550–564.
[28] J.P. Van Doormal, G.D. Raithby, Enhancements of the SIMPLE method for predicting incompressible fluid flows, Numer. Heat Transfer 7 (1984) 147–163.
[29] K. Walters, Recent developments in rheometry, in: P. Moldenaers, R. Keunings (Eds.), Proc. XIth Int. Congr. on Rheology, Theoretical and Applied Rheology, August 17–21, Elsevier, Brussels, Belgium, 1992, pp. 16–23.